DOI: 10.61782/fa.2023.0365

forum acusticum 2023

A METHOD FOR DIRECTIVITY ESTIMATION WITH A HIGH-ORDER NON-SPHERICAL MICROPHONE ARRAY

M. Hartenstein[1*] **P. Luizard**[2,3,4] **H. Moingeon**[1] **C. Pinhède**[2]
M. Pachebat[2] **C. Ollivon**[1] **F. Ollivier**[1] **F. Silva**[2]

[1] Institut Jean le Rond ∂'Alembert, Sorbonne Université, CNRS UMR 7190, Paris, France
[2] Aix Marseille Univ, CNRS, Centrale Marseille, LMA UMR 7031, Marseille, France
[3] Audio Communication Group, Technische Universität Berlin, Germany
[4] Univ. Grenoble Alpes, CNRS, Grenoble INP, GIPSA-lab, Grenoble, France

ABSTRACT

Far-field directivity measurements require sampling the sound field over a sphere. A high angular resolution is usually attained either by sequentially scanning the sphere rotating an half-circle antenna of microphone, or by placing a high number of microphones to cover the full sphere at once. The first method assumes repeatability of the source under study. This is not applicable to most natural sources, e.g. the human voice. The second approach requires a high number of microphones located on the surface of a sphere. Low cost Mems microphones allow to design microphone arrays with a large number of elements. However, it is cumbersome to precisely place these sensors on a sphere. The method proposed in this study allows to estimate far-field directivity from pressure measurements performed on a non-spherical surface, via a spherical wave propagation model. The robustness of the proposed method to experimental uncertainties (measurement noise and uncertainty on microphones location) is tested numerically using simulated sound fields. Array design guidelines are proposed after comparison of the quality of reconstruction for different array geometries and numbers of microphones.

Keywords: Directivity, Far-field, array processing

**Corresponding author*: *matthieu.hartenstein@sorbonne-universite.fr.*

1. INTRODUCTION

The far-field directivity of a sound source [1] describes the angular dependency of the source's far-field radiation. Directivity is valuable when analyzing the radiation of complex sound sources [2–9]. This quantity is also fundamental to incorporate sound sources in virtual audio environments [10]. In order to understand or reproduce accurately the radiated fields, 3 dimensional data with high frequency and spatial resolution are desirable.

Measuring directivities is not a trivial task. In case of measurements on controllable sources such as electro-acoustic devices, a few microphones can be used and the source can be rotated around an axis [11]. In [5], Flanagan performed measurements on a manikin to mimic the diffractive role of the human body. In [12], Leishman et al. proposed to apply this framework to human subjects, averaging directivities across subjects and phonemes to compensate for the violation of the source repeatability hypothesis. Given the significant role of body scattering on speech directivity above 1 kHz [8], physionomy impacts directivity. This prohibits averaging across subjects. Moreover, Refs [9] and [3] demonstrated that human speech directivity is strongly phoneme-dependent. Measurements of human speech directivity thus have to be performed at once. Most studies of human voice directivity [3, 6, 7] involved $2D$ measurements on an arc of microphones in the horizontal plane, sometimes on two arcs in the horizontal and sagittal planes. These valuable studies resulted in useful data in the context of radiated field analysis, even though the data are still frequency averaged, sometimes phoneme-averaged.

For more insight on human voice radiation, and in order to incorporate human voice in auralization frameworks, $3D$ directivity data is needed. However, conventional measurement sensors are expensive and bulky, which prohibits their use to build dense arrays of microphones. Ahrens and Bilbao [13] proposed to interpolate $3D$ directivities from data acquired on two perpendicular arcs of microphones. Refs [14, 15] propose to use interpolation methods to augment sparse measurement data. In [16], Ackermann et al. found that interpolation methods were more robust than the spherical harmonic decomposition in this same context. However, this last study was performed in the context of excessively sparse measurement data.

Thanks to the development of Mems microphones, it is now possible to design dense arrays of trustworthy sound pressure sensors. However, placing uniformly these sensors on an open sphere is cumbersome. In this work, we propose to place the sensors on an arbitrary measurement surface that surrounds the source, and to use a spherical wave propagation model in order to estimate the source directivity. The method is presented in Sec. 2. In Sec. 3, the performance of the method is assessed for a variety of array parameters and experimental uncertainties. Sec. 4 draws some recommendations on array designs that will lead to best efficiency of the proposed method.

2. METHOD

The technique presented in this work aims at estimating a far-field directivity based on measurements on a surface of arbitrary geometry. Subsection 2.1 reminds some theoretical background on spherical wave decomposition, subsection 2.2 draws a framework to estimate far-field directivities from measurements on far-field arrays of arbitrary geometries, and subsection 2.3 proposes a far-field criterion to choose a truncation order for the spherical wave decomposition.

2.1 Theoretical background

2.1.1 Spherical wave decomposition

The pressure field p due to a sound source centered at the origin of a spherical coordinate system can be expanded in the spherical wave basis [17, 18] as follows

$$p(r,\theta,\phi,k) = \sum_{n=0}^{+\infty} \sum_{m=-n}^{n} c_{mn}(k) h_n^{(2)}(kr) Y_n^m(\theta,\phi), \tag{1}$$

where (r,θ,ϕ) are the spherical coordinates of the observation point and k is the wavenumber. $Y_n^m(\theta,\phi)$ are the so-called spherical harmonics. $h_n^{(2)}(kr)$ are the spherical Hankel functions of the second kind. With the $e^{j\omega t}$ convention, they describe the radial dependency of a field which diverges from the center of the coordinate system. The $c_{mn}(k)$ are the coefficients of the pressure spherical wave decomposition.

2.1.2 Far-field directivity

In the far-field, as will be shown in subsection 2.3, the spherical Hankel functions follow a simple asymptote. For $kr \gg 1$, this allows to write [11]

$$\begin{cases} p(r,\theta,\phi,k) \approx D_\infty(\theta,\phi)\dfrac{e^{-jkr}}{kr}, \\ D_\infty(\theta,\phi) = \sum_{n=0}^{+\infty}\sum_{m=-n}^{n} c_{mn}(k) j^{n+1} Y_n^m(\theta,\phi), \end{cases} \tag{2}$$

where $D_\infty(\theta,\phi)$ is the far-field directivity function. This function describes the angular dependency of the sound pressure in the far-field. An example of directivity function is depicted in Figure 2. The method proposed in this work consists in estimating D_∞ from pressure measurements on an arbitrary surface. A similar method is described by Wu in [19]. However, the primary application of this method is near-field acoustical holography, even though prediction of radiated pressure fields is mentioned. In [11], Bellows and Leishman fit a spherical wave expansion to near-field measurements in order to estimate far-field directivities of loudspeakers. In this work, we propose to sample the pressure field in the far-field. This allows to truncate the spherical wave expansion at a lower order, as highlighted in subsection 2.3.

2.2 Estimation of the far-field directivity

2.2.1 Estimation of the spherical wave coefficients

In practice, the pressure field can be observed at a discrete set of Q microphone positions (r_q,θ_q,ϕ_q) placed on a surface that encloses the source, such as the ones shown in Figure 3. The measurements at a given frequency can then be compiled in a vector of frequency-domain measured pressures $\mathbf{p}$. Expanding these measured pressures

as in (1) and flattening the spherical wave orders n and degree m according to the Ambisonic Channel Number sequence [20] allows to write the following linear system of equations

$$\begin{cases} \mathbf{p} = \mathbf{H}\mathbf{c} \\ \mathbf{H} = [h_n(kr_q)Y_n^m(r_q, \theta_q, \phi_q)] \\ \mathbf{c} = [c_{mn}(k)] \end{cases} \tag{3}$$

For numerical purpose, the expansion is truncated at order N, which will be discussed in Sec. 2.3. Equation (3) has Q lines and $(N+1)^2$ columns. We work in the over-determined case where $Q \geq (N+1)^2$.

The spherical wave coefficients can eventually be estimated in a ℓ_2-regularized least-squares fashion [21]

$$\hat{\mathbf{c}} = \left(\mathbf{H}^{\mathrm{H}}\mathbf{H} + \lambda\mathbf{I}\right)^{-1}\mathbf{H}^{\mathrm{H}}\mathbf{p}, \tag{4}$$

where $\mathbf{I}$ is the $(N+1)^2 \times (N+1)^2$ identity matrix and λ is a regularization coefficient (chosen ad-hoc and fixed in this work).

2.2.2 *Computation of the far-field directivity*

Once the spherical wave coefficients have been estimated, an estimate of the far-field directivity function can be computed on any angular grid (θ_l, ϕ_l) using a truncated version of equation (2)

$$D_\infty^{\mathrm{est}}(\theta_l, \phi_l) = \sum_{n=0}^{N}\sum_{m=-n}^{n} \hat{c}_{mn}(k) j^{n+1} Y_n^m(\theta_l, \phi_l). \tag{5}$$

2.3 Choice of a truncation order

In the literature [11, 22], spherical waves and spherical harmonics expansions are generally truncated at an order related to the largest kr of study, $N \approx (kr)_{max}$. This criterion is appropriate when performing near-field measurements. In the near-field, higher order spherical Hankel functions have a stronger amplitude than lower orders, see Figure 1 for $kr < 1$. High order spherical waves are thus preponderant and need to be modelled. In the far-field, also called active field, high order Hankel functions have significantly decayed, see Figure 1 when $kr > 1$. In the far-field, the spatial variations of the field are thus smoother, and lower truncation orders are needed to model the measurements.

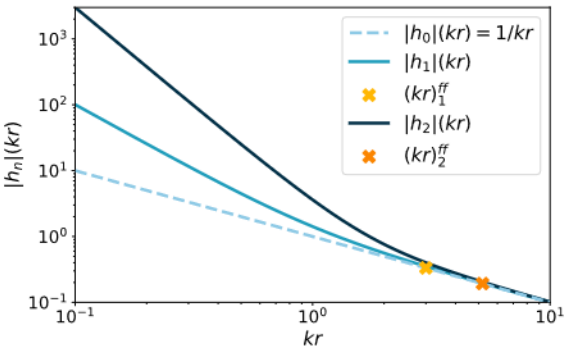

Figure 1: Behavior of the three first Hankel functions magnitude and illustration of the far-field truncation order criterion. In the far-field, Hankel functions decay in $1/(kr)$. The activation values $(kr)_n^{\mathrm{ff}}$, computed via (8) with $\eta = 3$ are represented as crosses. Above these values of kr, the corresponding Hankel functions are close enough to their far-field asymptotes, and can be assumed to significantly contribute to the far-field.

The absolute value of spherical Hankel functions presents the following near and far-field asymptotes [17]

$$\begin{cases} |h_n^{(2)}|(kr \ll 1) \approx \dfrac{1}{(kr)^{(n+1)}}\dfrac{(2n)!}{2^n n!} \\ |h_n^{(2)}|(kr \gg 1) \approx \dfrac{1}{kr}. \end{cases} \tag{6}$$

These asymptotical forms explain the behavior observed in Figure 1 and described in the first paragraph. At a given order n, the near and far-field asymptotes cross at a particular value of kr

$$(kr)_n^c = \left(\frac{(2n)!}{2^n n!}\right)^{(1/n)} \tag{7}$$

We choose to define a cut-on value of kr above which spherical waves of order n contribute to the far-field as

$$(kr)_n^{\mathrm{ff}} = \eta (kr)_n^c, \tag{8}$$

where η is a safety coefficient. Spherical waves of order n contribute to the far-field only if $kr > (kr)_n^{\mathrm{ff}}$. If measurements were performed at radii higher than r_{min}, for a given order n, there exists a minimum frequency

$$f_n^{\mathrm{ff}} = c_0 \frac{(kr)_n^{\mathrm{ff}}}{2\pi r_{\mathrm{min}}} \tag{9}$$

above which the spherical waves of order n will contribute to the measuremed pressure. In other words, a given order n needs to be activated in the spherical wave model (equation (3)) only for frequencies above f_n^{ff}. Note that $(kr)_n^{\text{c}}$ increases with n, as can be read from equation (7). As a result, $(kr)_n^{\text{ff}}$ and the activation frequency f_n^{ff} increases with the order n (see Figure1). At a given frequency f, only orders n for which $f_n^{\text{ff}} > f$ need to be activated, which provides the truncation criterion.

3. NUMERICAL VALIDATION

Numerical simulations were performed in order to test the method described in Sec. 2. The framework and parameters of the simulations are presented Sec. 3.1. The results of the simulations are exposed Sec. 3.2.

3.1 Framework

3.1.1 Source under study

In the simulations, a spherical cap source model was used to test the method. This model is described Figure 2. A sphere radius of 8.5 cm and an aperture radius of 2 cm was used. An axis-symmetrical Boundary Element Method (BEM) model of this source was built using the open source software OpenBEM [23] on a frequency range of approximately $[70, 7000]$ Hz. Note that the fields radiated by the spherical cap could have been computed with an analytical model based on a spherical wave expansion [1, 17]. The choice of BEM synthesis over the analytical solution, despite its higher numerical burden, was motivated by the consideration of using different methods for synthesis and analysis of the acoustic fields. Moreover, the BEM tool will also allow to study more complex sources in future studies. A convergence study comparing the BEM results with the analytical model of the spherical cap showed that 10 elements per shortest wavelengths were sufficient to discretize the source surface. The source model was used to compute both the pressure measurements $\mathbf{p}$ and a vector $\mathbf{D}_\infty^{\text{ref}}$ of far-field directivity function values sampled on a reference angular grid, see Figure 3.

3.1.2 Variable parameters

The performance of the method was assessed for different array configurations. The geometries under test are shown Figure 3. Several array extents and number of sensors were used in the simulations.

Pressure measurements were contaminated with a Gaussian additive noise such that the L2-averaged signal-

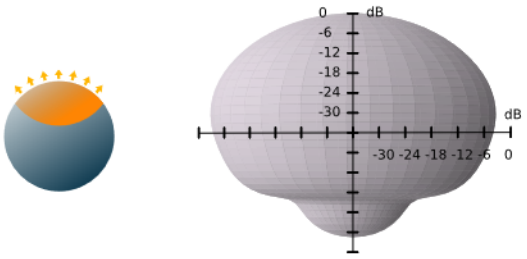

Figure 2: Left : Illustration of the spherical cap model. The blue part of the sphere remains still, while the orange part vibrates uniformly. A spherical harmonic based analytical representation of this source is available, see *e.g.* [1, 17]. Moreover, this simple source has been proposed to model speech directivity, *e.g.* in [5]. Right : the far-field directivity magnitude of a spherical cap of sphere radius 8.5 cm and aperture 2 cm, at 2kHz, represented as a balloon plot. The radius of the balloon plot gives the magnitude of the far-field directivity, in dB - ref. max.

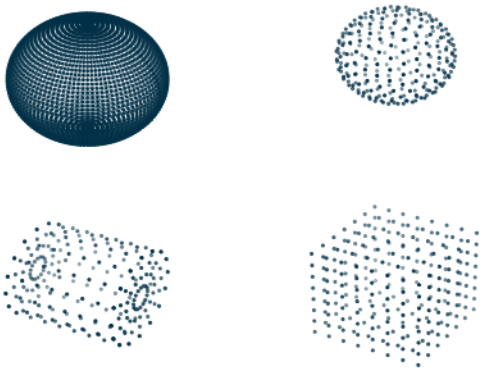

Figure 3: Array geometries used in the experiments. Top left : reference angular grid (spherical geometry, equal-angle distribution with 51 elevation points and 103 azimutal points). Top right : spherical array (minimum energy point distribution, see [24]), Bottom left : cylindrical array. Bottom right : cuboïd array. The source was radiating in the vertical direction.

Table 1: Activation frequencies used to define the truncation order according to equation (9). The values are shown for a 1.5m radius array. For a 0.5m radius array, they should be multiplied by 3 (cf. equation (9)). A preliminary study showed that using truncation orders higher than 12 does not improve the accuracy of the method for this source. This gave a maximal truncation order.

Order n	f_n^{ff} (Hz)
0	0
1	82
2	142
3	202
4	262
5	322
6	383
7	443
8	503
9	563
10	623
11	684
12	744

to-noise ratio on the array was 30 dB SNR. Uncertainty in the sensor locations was introduced by disturbing the Cartesian sensor locations $(x_q, y_q, z_q) = (r_q \cos(\phi_q) \sin(\theta_q), r_q \sin(\phi_q) \sin(\theta_q), r_q \cos(\theta_q))$ in the model matrix $\mathbf{H}$ of equation (3) with a Gaussian additive noise such that the L2-averaged position error on the array was 5 millimeters.

3.1.3 Performance metric

For each set of array and experimental parameters, 100 Monte-Carlo experiments were run. For each run, the spherical wave coefficients are estimated using equation (4). An ad-hoc regularization parameter $\lambda = 10^{-4}$ was chosen prior to the Monte-Carlo runs. To allow for comparison of performance between different array parameters, this same regularization level was used for all parameters and frequencies. The frequency dependent truncation order was chosen using the far-field criterion defined in Sec. 2, see Table 1. A vector $\mathbf{D}_\infty^{\text{est}}$ of estimates of the directivity function values on the reference angular grid was then computed using equation (5).

The relative L2-averaged error on the reference spherical grid was computed

$$E = \frac{||\mathbf{\Omega} \left(\mathbf{D}_\infty^{\text{est}} - \mathbf{D}_\infty^{\text{ref}}\right)||_2}{||\mathbf{\Omega} \mathbf{D}_\infty^{\text{ref}}||_2}, \tag{10}$$

where $\mathbf{\Omega}$ is a diagonal matrix of the square-root of weights corresponding to a 0-th order integration on the reference equal-angle grid. The average and standard deviation of the relative error E were computed over the Monte-Carlo runs.

3.2 Results

3.2.1 Influence of experimental uncertainties

Figure 4 shows typical error curves for fixed array parameters. Without microphones location uncertainty (light blue curve), the spatially averaged L2-error is kept below 12% on the whole frequency range, excluding three error peaks around 300, 650 and 1000 Hz. Less pronounced peaks are visible on this same curve at higher frequencies. These peaks are likely due to a ill-conditioned matrix $\mathbf{H}$ in equation (3). With microphone location uncertainty (dark blue curve), the behavior of the error curve is the same as without location uncertainty below 600 Hz : the error is kept fairly low, with two isolated peaks at 300 and 650 Hz. From 600 Hz on the same curve, the error starts to increase with frequency, as the mean position uncertainty (5 mm) becomes more and more comparable to the acoustic wavelength. The mean directivity estimation error grows from about 20% at 1 kHz to 60% at 7 kHz on the dark curve (obtained with microphone location uncertainty). In this frequency range, the microphone location uncertainty is the most significant source of error, dominating the sensor noise contribution and the peaks due to ill-conditioning seen on the lighter curve. Additionally, the error deviation with microphone location uncertainty grows from around $\pm 3\%$ at 600 Hz to around $\pm 25\%$ at 7 kHz, while it was kept below 1% without microphone location uncertainty.

3.2.2 Influence of the array parameters

Figure 5a shows the evolution of the directivity estimation error for two different array extents. Below 900 Hz, the errors obtained with the two arrays are comparable, the smaller array (light curve) being slightly more efficient than the larger one (dark curve). Between 900 Hz and 2 kHz, the discrepancies are more noticeable, but not critical (around 5% higher error for the larger one). Above 2 kHz, the smaller array leads to higher average error than the larger one. Above 2-3 kHz, the uncertainty in performance is also critically higher for the smaller array. The

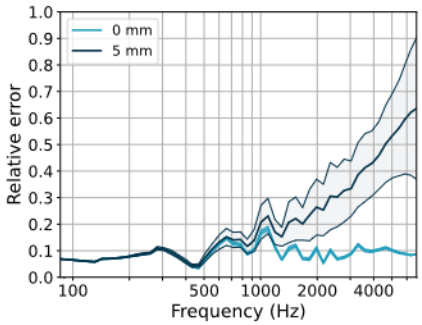

Figure 4: Evolution with frequency of the error defined in equation (10), averaged across 100 realizations. Measurements with around 256 microphones uniformly distributed on the surface of a cube of half-extent 1.5 m. Measurement noise (30 dB SNR) included. Dark blue : 5 mm uncertainty in the microphones location. Light blue : no geometrical uncertainty. Standard deviations are represented as transparent zones.

poorer performance of smaller arrays at higher frequencies can be explained by higher spherical wave truncation orders being needed for a smaller array.

Figure 5b shows the evolution in performance of the method for 256 and 1024 microphones. Below 800 Hz, increasing the number of sensors does not seem to improve the results. However, with 1024 sensors (dark curve), the high frequency increase in error mentioned 3.2.1 starts only around 2 kHz, while it starts around 1 kHz with 256 sensors (light curve). From 1.5 kHz, using 1024 sensors allows to significantly reduce the average error. In this same frequency range, the error uncertainty is also reduced using more microphones. This shows that over-determination in (3) increases the performance of the method.

At last, Figure 5c shows the evolution of the error for different array shapes. Below 2 kHz, the three geometries have similar performance, although the cuboïd geometry (yellow curve) presents higher error peaks than the cylindrical (light blue) and spherical (dark blue) ones. Remind that these peaks might be due to ill-conditioning of the inverse problem (3). It is very likely that increasing the regularization strength at the peak frequencies will attenuate the error peaks. Above 2 kHz, the spherical geometry (dark blue curve) leads to the lowest average error. The cylindrical (light blue) and cuboid (yellow) geometries give very similar average errors in this frequency range. The three geometries lead to similar levels of uncertainty in the estimated directivity, with slightly lower ones for the spherical geometry, and slightly higher uncertainties for the cuboid one at higher frequencies.

4. CONCLUSIONS

In this work, a method for estimating the far-field directivity of a sound source from measurements on a non-spherical array is proposed. The method applies to far-field measurements, which allows to define a more convenient truncation order than the high truncation orders needed when processing near-field measurements.

Monte-Carlo simulations were performed in order to quantify the robustness of the method to experimental conditions. The main source of error and discrepancy was shown to be the uncertainty in sensor location. This source of error is unavoidable when working with large microphone arrays. In practice, some methods exist to recover the sensors location from acoustic measurements [25–27]. They lead to levels of uncertainties in the order of magnitude as the ones used in this work.

An analysis of the efficiency of the method was performed, for varying array parameters. It was shown that a large number of sensors leads to lower errors and more stable performance. These results underlined that over-determination of the inverse problem (3) is key to increase the robustness of the method to experimental uncertainties. Moreover, it was highlighted that performing far-field measurements allows to minimize the number of spherical wave coefficients to be retrieved, which increases the over-determination of this same inverse problem. This leads to better performance for larger arrays than for smaller ones.

The spherical array design was found to be the optimal one. However, crafting an uniformly distributed spherical array compounded of hundreds of microphones is infeasible in practice. It is noticeable that the cuboïd and cylindrical arrays lead to very similar performance in presence of experimental uncertainties. Note that in [11], Bellows and Leishman observe that arrays of most spherical geometries have best performance in the context of near-field measurements, and find that a cylindrical geometry behaves better than a cuboïd one. However, they don't include any experimental uncertainties in their simulations.

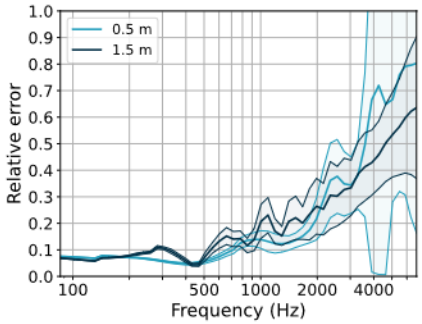

(a) Influence of the extent. Fixed geometry (cuboïd) and number of sensors (around 256).

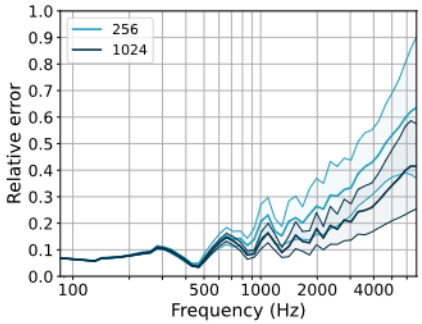

(b) Influence of the number of sensors. Fixed geometry (cuboïd) and half-extent (1.5 m).

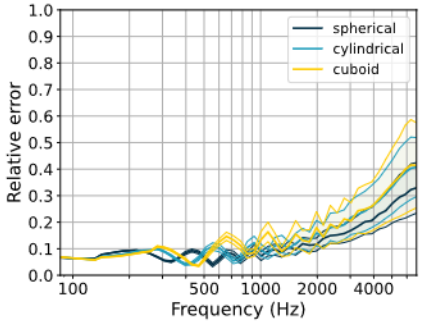

(c) Influence of the geometry. Fixed half-extent (1.5m) and number of sensors (around 1024).

Figure 5: Evolution with frequency of the error defined in equation (10), averaged across 100 realizations. Measurement noise (30 dB SNR) and microphone position uncertainty (5 mm standard deviation) were included in the simulations.

5. ACKNOWLEDGMENTS

This work is part of the Rayovox project, a collaboration between Laboratoire de Mécanique et d'Acoustique (LMA, Marseille) and Institut Jean le Rond ∂'Alembert (Paris). The project is funded by the French National Research Agency (ANR-21-CE42-0017, 2021-25).

6. REFERENCES

[1] B. Rafaely, *Fundamentals of Spherical Array Processing*, vol. 8 of *Springer Topics in Signal Processing*. Springer Berlin Heidelberg, 2015.

[2] M. Pezzoli, A. Canclini, F. Antonacci, and A. Sarti, "A comparative analysis of the directional sound radiation of historical violins," *The Journal of the Acoustical Society of America*, vol. 152, pp. 354–367, July 2022.

[3] P. Kocon and B. B. Monson, "Horizontal directivity patterns differ between vowels extracted from running speech," *The Journal of the Acoustical Society of America*, vol. 144, July 2018.

[4] N. R. Shabtai, G. Behler, M. Vorländer, and S. Weinzierl, "Generation and analysis of an acoustic radiation pattern database for forty-one musical instruments," *The Journal of the Acoustical Society of America*, vol. 141, pp. 1246–1256, Feb. 2017.

[5] J. L. Flanagan, "Analog Measurements of Sound Radiation from the Mouth," *The Journal of the Acoustical Society of America*, vol. 32, no. 12, p. 8, 1960.

[6] H. K. Dunn and D. W. Farnsworth, "Exploration of Pressure Field Around the Human Head During Speech," *The Journal of the Acoustical Society of America*, vol. 10, no. 184, p. 16, 1939.

[7] A. Quélennec and P. Luizard, "Pilot study on the influence of spatial resolution of human voice directivity on speech perception," *Acta Acustica*, vol. 6, p. 10, 2022.

[8] M. Brandner, R. Blandin, M. Frank, and A. Sontacchi, "A pilot study on the influence of mouth configuration and torso on singing voice directivity," *The Journal of the Acoustical Society of America*, vol. 148, pp. 1169–1180, Sept. 2020.

[9] C. Pörschmann and J. M. Arend, "Investigating phoneme-dependencies of spherical voice directivity

patterns," *The Journal of the Acoustical Society of America*, vol. 149, pp. 4553–4564, June 2021.

[10] S. Bilbao, J. Ahrens, and B. Hamilton, "Incorporating source directivity in wave-based virtual acoustics: Time-domain models and fitting to measured data," *The Journal of the Acoustical Society of America*, vol. 146, pp. 2692–2703, Oct. 2019.

[11] S. D. Bellows and T. W. Leishman, "Obtaining far-field spherical directivities of guitar amplifiers from arbitrarily shaped arrays using the Helmholtz equation least-squares method," in *Proc. Mtgs. Acoust.*, vol. 42, (held online), Dec. 2020.

[12] T. W. Leishman, S. D. Bellows, and C. M. Pincock, "High-resolution spherical directivity of live speech from amultiple-capture transfer function method," *The Journal of the Acoustical Society of America*, vol. 149, no. 3, p. 18, 2021.

[13] J. Ahrens and S. Bilbao, "Computation of Spherical Harmonics Based Sound Source Directivity Models from Sparse Measurement Data," in *Proc. Forum Acusticum*, (held online), p. 8 pages, 2020.

[14] C. Porschmann and J. M. Arend, "A Method for Spatial Upsampling of Directivity Patterns of Human Speakers by Directional Equalization," in *Proc. DAGA*, (Rostock, Germany), p. 5, 2019.

[15] J. Ahrens and S. Bilbao, "Interpolation and Range Extrapolation of Sound Source Directivity Based on a Spherical Wave Propagation Model," in *Proc. IEEE Int. Conf. Acoust. Speech Signal Process.*, (Barcelona, Spain), pp. 4662–4666, IEEE, May 2020.

[16] D. Ackermann, F. Brinkmann, F. Zotter, M. Kob, and S. Weinzierl, "Comparative evaluation of interpolation methods for the directivity of musical instruments," *EURASIP Journal on Audio, Speech, and Music Processing*, vol. 2021, p. 36, Oct. 2021.

[17] E. G. Williams, "Chapter 6 - Spherical Waves," in *Fourier Acoustics* (E. G. Williams, ed.), pp. 183–234, London: Academic Press, Jan. 1999.

[18] J. Gomes, J. Hald, P. Juhl, and F. Jacobsen, "On the applicability of the spherical wave expansion with a single origin for near-field acoustical holography," *The Journal of the Acoustical Society of America*, vol. 125, pp. 1529–1537, Mar. 2009.

[19] S. F. Wu, *The Helmholtz Equation Least Squares Method: For Reconstructing and Predicting Acoustic Radiation*. New York, NY: Springer New York, 2015.

[20] M. Chapman, W. Ritsch, T. Musil, I. Zmölnig, H. Pomberger, F. Zotter, and A. Sontacchi, "A Standard for Interchange of Ambisonic Signal Sets Including a File Standard with Metadata," in *Proc. Ambisonics Symposium*, (Graz, Austria), p. 27, Jan. 2009.

[21] P. C. Hansen, *Discrete Inverse Problems: Insight and Algorithms*. No. 7 in Fundamentals of Algorithms, Philadelphia: Society for Industrial and Applied Mathematics, 2010.

[22] F. Jacobsen, G. Moreno-Pescador, E. Fernandez-Grande, and J. Hald, "Near field acoustic holography with microphones on a rigid sphere," *The Journal of the Acoustical Society of America*, vol. 129, pp. 3461–3464, June 2011.

[23] V. C. Henríquez and P. M. Juhl, "OpenBEM - An open source Boundary Element Method software in Acoustics," in *Proc. Internoise*, (Lisbon, Portugal), p. 10, 2010.

[24] I. H. Sloan and R. S. Womersley, "Extremal Systems of Points and Numerical Integration on the Sphere," *Advances in Computational Mathematics*, vol. 21, pp. 107–125, July 2004.

[25] C. Vanwynsberghe, P. Challande, F. Ollivier, J. Marchal, and R. Marchiano, "Geometric calibration of very large microphone arrays in mismatched free field," *The Journal of the Acoustical Society of America*, vol. 145, pp. 215–227, Jan. 2019.

[26] R. Wang, Z. Chen, and F. Yin, "A constrained total least squares calibration method for distributed microphone array," *Applied Acoustics*, vol. 140, pp. 188–197, Nov. 2018.

[27] T.-K. Le, N. Ono, T. Nowakowski, L. Daudet, and J. De Rosny, "Experimental validation of TOA-based methods for microphones array positions calibration," in *Proc. IEEE Int. Conf. Acoust. Speech Signal Process.*, (Shanghai, China), pp. 3216–3220, IEEE, Mar. 2016.